



Precise orbits of the Lunar Reconnaissance Orbiter from radiometric tracking data

Anno Löcher¹ · Jürgen Kusche¹

Received: 23 July 2017 / Accepted: 30 January 2018
© Springer-Verlag GmbH Germany, part of Springer Nature 2018

Abstract

Since 2009, the Lunar Reconnaissance Orbiter (LRO) acquires images and altimetric profiles of the lunar surface. Assembling these data to maps and terrain models requires the precise knowledge of the spacecraft trajectory. In this contribution, we present 5 years of LRO orbits from radiometric data processed with a software tailored to this mission. The presented orbits are the first independent validation of the LRO science orbits from NASA and are available for public use. A key feature of our processing is the elaborate treatment of model and observation errors by empirical parameters and an adaptive data weighting by variance component estimation. The quality of the resulting orbits is assessed by analyzing overlapping arcs. For our solution based on arcs of 2.5 days, such analysis yields a mean error of 2.81 m in total position and 0.11 m in radial direction. It is shown that this result greatly benefits from the adaptive data weighting, reducing the error by 2.54 and 0.13 m, respectively. Unfortunately, the precision achieved varies strongly, dependent on the view onto the orbital ellipse which changes with the lunar cycle. To mitigate this dependency, the arc length was extended in steps up to 10.5 days, leading in the best case to a further improvement of 0.80 m.

Keywords Lunar Reconnaissance Orbiter · Radiometric ranging · Precise orbit determination

1 Introduction

The Lunar Reconnaissance Orbiter (LRO, Chin et al. 2007) is one of the robotic missions intended to prepare the human return to the Moon announced by the US government in 2004. Its principal task is a mapping of the Moon in order to support the identification of future landing sites. More precisely, LRO shall provide a detailed description of the lunar topography to assess both the feasibility of a landing maneuver and the illumination environment for the subsequent stay. Further tasks assigned to the mission include the characterization of the lunar radiation environment, the monitoring of the lunar surface temperature and the detection of water ice.

Designed and assembled entirely at NASA's Goddard Space Flight Center (GSFC), LRO was launched on June 18, 2009, from Cape Canaveral and entered lunar orbit on June 23, 2009. Its scientific payload consists of six instruments, among them the Lunar Reconnaissance Orbiter Camera

(LROC, Robinson et al. 2010) and the Lunar Orbiter Laser Altimeter (LOLA, Smith et al. 2010). The LROC unit bundles three cameras with different characteristics: a wide-angle camera with multispectral capabilities resolving 100 m in visible light and two narrow-angle cameras having a resolution of 50 cm; both values refer to the typical altitude of LRO of 50 km. The LOLA instrument is a five-beam laser altimeter throwing an X-shaped pattern to the Moon with an individual footprint size of approximately 5 m from 50 km altitude. The accuracy of the measured range is defined by the resolution of the LOLA timing system and is reported to be 10 cm. Both instruments were switched on soon after LRO arrived its lunar orbit and are still operational. At the time of writing (June 2017), more than 4 million LROC images have been released by NASA's Planetary Data System (PDS), and several billion altimeter ranges are stored in the LOLA PDS node.

To fully exploit the accuracy of these data, orbits of similar accuracy would be needed. When the LRO mission was prepared, this was beyond any possibilities, the main obstacle being the poor knowledge of the lunar gravity field at this time. Furthermore, the LRO tracking had to be realized with limited resources (Mazarico et al. 2012). Unlike the Lunar

✉ Anno Löcher
loecher@geod.uni-bonn.de

¹ Institut für Geodäsie und Geoinformation, Universität Bonn,
Nussallee 17, 53115 Bonn, Germany

Prospector mission in 1998–1999, the LRO project could not rely on the NASA Deep Space Network (DSN) with its large and powerful antennas, but got its own, smaller antenna at White Sands, New Mexico. Additional observation time was provided by contracts with four radio stations in Hawaii, Australia and Europe associated with the commercial Universal Space Network (USN). The observations produced at all stations are Doppler range rates and two-way ranges at S-band frequencies. In parallel, White Sands handles the data downlink of the science data in the Ka-band.

The performance of the LRO ground network was initially believed to be sufficient for an orbit accuracy of 500 m which was the requirement for the navigation orbit. For the science orbit, however, the requirements were set to the more demanding values of 50–100 m in total position and 1 m in radial direction (Vondrak et al. 2010). To solve this contradiction, LRO was additionally equipped with an Earth-directed optics connected by a fiber cable with the detector of the LOLA altimeter. The spacecraft was thus prepared for one-way ranging from laser stations capable to reach the Moon. In the following years, ten stations of the International Laser Ranging Service (ILRS) contributed regularly to the LRO tracking until the campaign ended in 2014.

The laser ranges to LRO have gained some attention in the laser ranging community, due to the novelty of the data type and the related challenges in data modeling (Bauer et al. 2017; Mao et al. 2017). They did not gain, however, the importance initially attributed to them, because the radiometric data turned out to be better than expected. The NASA science orbits computed at GSFC (Mazarico et al. 2012) did not use the laser ranges. Instead, the radiometric data were supplemented by altimetric crossovers, a technique inherited from the Mars Global Surveyor, likewise equipped with a laser altimeter. Even the first release of these orbits could achieve an accuracy level around 20 m in total position and 1 m radially, assessed by an analysis of overlaps of adjacent arcs. In 2013, the orbits were reprocessed after the completion of the Gravity Field and Interior Laboratory (GRAIL, Zuber et al. 2013) mission which provided lunar gravity fields of a quality much improved compared to earlier models. The accuracy of the LRO science orbits is since then reported to be around 10 m in total position and 0.5 m in radial direction (Mazarico et al. 2013, 2017). The altimetric crossovers were abandoned with the GRAIL fields, since their impact became small with the improvement achieved in the force modeling (Mazarico et al. 2017).

Given the last-mentioned numbers, the task of orbit determination could be considered as solved for LRO. It is true, however, that these numbers rather describe the inner consistency of the orbits than their accuracy in absolute terms: Other orbits may differ but show the same differences in their overlaps. Indeed, there are few orbit products suited for such comparisons. Up to now, the analysis of radiometric data

is done almost exclusively by NASA, namely by the GSFC Flight Dynamics Facility (FDF, Nicholson et al. 2010) for the navigation orbits and the LOLA Science Team at GSFC for the science orbits. Only Maier and Baur (2016) computed radiometric orbits outside NASA but using the GSFC software GEODYN which is the tool applied for the official science orbits.

In this paper, we present an independent orbit solution from 5 years of radiometric tracking which are made publicly available for the analysis of LRO instrument data. Except for some small gaps caused by maneuvers, it covers the full period from June 23, 2009, to September 9, 2014, corresponding to the mission phases Commissioning (CO), Nominal Mission (NO), Science Mission (SM) and the first 2 years of the Extended Science Mission (ES). The development of these orbits was done in the framework of a project on lunar reference systems funded by the German Research Foundation (DFG) with partners active in the analysis of Lunar Laser Ranging (LLR) and the processing of LRO imaging and altimetry. An earlier state of this work was reported in Löcher et al. (2017) including a demonstration for a validation procedure based on the localization of a LLR reflector from LRO orbits and LRO images. In the present paper, we focus exclusively on orbit determination, while we look forward to the application of our orbits for the geolocation of the LROC images and the LOLA ranges.

The paper is organized as follows. Section 2 gives a short overview over the characteristics of the LRO orbit and the observation geometry. Sections 3 and 4 describe the tracking data and the orbit determination procedure. In Sects. 5 and 6 the results are presented and discussed.

2 Orbit and observation geometry

LRO orbits the Moon in a polar orbit as required for complete mapping, including potential polar landing sites. Over the years, this orbit has undergone several changes. After its arrival at the Moon, LRO was placed in a stable (“quasi-frozen”) 30×216 km elliptical orbit with its periapsis near the lunar south pole. This maneuver marked the beginning of the three-month CO phase during which the instruments were switched on and tested. On September 25, 2009, LRO transitioned for the regular mapping operation to a near-circular orbit with an average altitude of 50 km (Fig. 1, top). This orbit, highly sensitive to the rich details of the lunar gravity field, was maintained over 2 years by monthly station-keeping (SK) maneuvers associated with a rapid loss of fuel. At the end of this period, in August and November 2011, LRO was maneuvered twice into a slightly elliptical orbit with a periapsis of 21 km to have a closer look onto the Apollo landing sites (Keller et al. 2016). On December 11, 2011, LRO returned for the rest of its lifetime to the quasi-

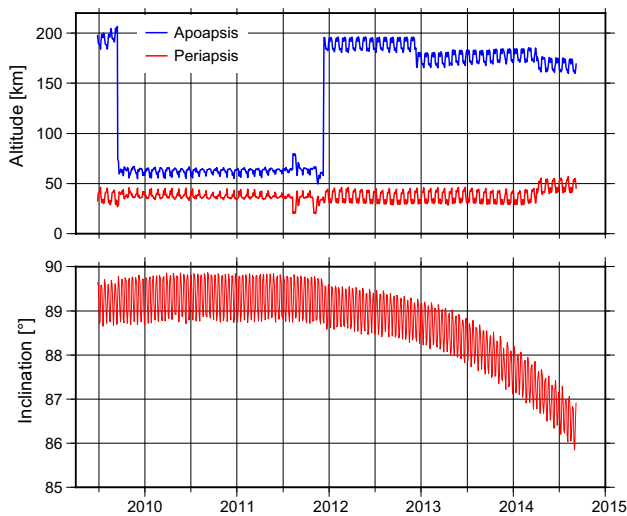


Fig. 1 Apoapsis, periapsis and inclination of the LRO orbit in the period considered in this study

frozen elliptical orbit. Since then, the apoapsis was lowered twice, first on December 13, 2012, to observe the impact of the GRAIL satellites on the lunar surface, and again on April 3, 2014, in preparation on a lunar eclipse. Since the return to the elliptical orbit, a slow decrease of the inclination is observed, dropping to 86° until late 2015 (Fig. 1, bottom).

In addition to the SK maneuvers, so-called δH events are scheduled twice each month to unload excessive angular momentum from LRO's reaction wheels. Another regular, less frequent event is a yaw flip maneuver performed twice per year in order to keep the single solar panel on the sunlit side of the orbiter. Each of these maneuvers interrupts the free fall motion of the spacecraft such that the maximum arc length for which a dynamical orbit can be integrated is limited to about 14 days.

Both in the elliptical and in the circular orbit, the revolution time of LRO is approximately 2 h. Except for a few days per month, LRO is visible from the Earth half this time, otherwise hidden on the lunar far side. The time an Earth-based

station can acquire observations is thus partitioned in periods of 1 h (referred to as “passes” hereafter) each followed by an idle time of the same duration. Due to the rotation of the Earth, a single station can observe only a limited number of such passes in a row, afterward a station farther west must become operational. Table 1 shows how the observation time is thus distributed across the LRO tracking network. It is obvious that the USN facilities are scheduled as supporting stations because White Sands alone accounts for nearly 60% of all observations. Part of this inequality is due to the fact that the average observation time per pass is shorter at the USN stations, in many individual cases just 30 min. As a consequence, the observed part of the orbit amounts only to 36%, the theoretical maximum being 50%.

Another periodical effect is caused by the motion of the Moon around the Earth. Since the orbital plane of LRO is space-fixed, the appearance of the orbital ellipse on the Earth is changing with a period of 14 days. From the perspective of the spacecraft, this is described by the β angle (of the Earth), the elevation of the Earth above the orbit plane. The case $\beta = 90^\circ$ means that the orbital ellipse is seen as a circle (“face-on” geometry), at $\beta = 0^\circ$, it is seen as a line (“edge-on” geometry). It is known from previous studies (and will be confirmed in the following) that this changing geometry has a significant influence on the result of the orbit reconstruction.

3 Tracking data

In the period considered in this study, the LRO network produced an observation volume of nearly 17000 hours (see Table 1). The data are distributed via the Planetary Data System in small binary files each covering a period of 5 min with one data record per 5 s. The critical entries in the epochs are a time tag, the two-way round-trip time of a test signal and a Doppler count. Typically both observation types are present (or both are flagged out as invalid) so that the data amount is roughly the same in both cases.

Table 1 Hours of data acquired by the LRO ground network from June 21, 2009, to September 9, 2014

Station ID	Location	Total observation time		Mean pass length
		Hours	%	
119, 117	White Sands, New Mexico, USA	9765.8	58.9	0.87
105, 115	South Point, Hawaii, USA	1156.8	7.0	0.65
103	Dongara, Australia	3166.9	19.1	0.63
126, 127	Kiruna, Sweden	1844.0	11.1	0.57
128, 129	Weilheim, Germany	633.1	3.8	0.45
Total time network		16,566.6	100.0	
Mission time elapsed		45,744.0		
Mission time observed			36.2%	

The statistics is based on the start/end time tags of the tracking data files as listed in index.tab in the LRO Radio Science Archive. Uncovered periods up to 5 min and gaps within the files were ignored

The handling of the two-way observations is straightforward because it is similar to the processing of laser ranging data. First, a multiplication by the speed of light yields ranges, then corrections for station motion, atmospheric and relativistic delays have to be applied. Here, the atmospheric corrections include both a tropospheric and a ionospheric part. For both we use models from GNSS, for the troposphere the Vienna Mapping Function (Böhm et al. 2006), for the ionosphere the IONEX TEC maps from the International GNSS Service (IGS). Unlike two-way laser ranges, radiometric ranges are biased by nature due to delays in the station electronics and in the satellite transponder which correspond to several 100 m in S-band. In addition, the ranges to LRO are known to have biases in the time tags (Mazarico et al. 2012; Słojkowski 2014). Since the exact values of these biases are unknown, they have to be estimated in the analysis.

In case of the Doppler counts, the conversion to a geometrical observable is more complicated. Essentially we follow the description of the tracking data (GSFC 2010), where the user is guided to convert them into range rates which is the typical approach. To do so, the following equation has to be applied:

$$\dot{r} = \frac{c}{B} \left(\frac{N(t_i) - N(t_{i+1})}{t_{i+1} - t_i} + 2.4 \times 10^8 \text{ s}^{-1} \right), \quad (1)$$

where $N(t_i)$ and $N(t_{i+1})$ denote the Doppler counts at subsequent epochs, c the speed of light, and B a frequency-dependent constant. The resulting quantity \dot{r} is the mean range rate in the interval $[t_i, t_{i+1}]$. As derived in Löcher et al. (2017) (and repeated here for completeness), a slight rearrangement of Eq. 1 is sufficient to obtain instead the range increment

$$\begin{aligned} \int_{t_i}^{t_{i+1}} \dot{r}(t) dt &= \dot{r}(t_{i+1} - t_i) \\ &= \frac{c}{B} \left(N(t_i) - N(t_{i+1}) + 2.4 \times 10^8 (t_{i+1} - t_i) \right). \end{aligned} \quad (2)$$

After summing up these increments, the final outcome is a biased range which can be treated nearly the same way as the two-way ranges. Differences exist in the ionospheric delay which has opposite signs in both range types and in the biases caused by instrumental errors: In case of the Doppler observations, there is a known time bias in the early data from White Sands, and the Doppler counts from the USN stations are biased throughout the mission (Mazarico et al. 2012; Słojkowski 2014). Since we use integrated Doppler counts, the latter biases appear as drifts which means that, for the USN stations, bias and drift parameters must be estimated.

Using Doppler ranges instead of range rates renders further processing more convenient in almost every regard. For instance, it enables a direct comparison of residuals which is

crucial for an adapted data weighting (see Sect. 4). A drawback is that the Doppler counts can be corrupted by jumps, very similar to the phase observations in GNSS. If converting the Doppler counts to range rates, such a jump appears as single outlier which can be detected and removed. In the Doppler ranges, however, it appears again as jump which cannot be repaired other than by splitting the pass. Thus, the ranges must be checked very early in the processing which may mean that some smaller jumps are not detected.

4 Orbit determination strategy

The LRO tracking data, processed as described above, form a pool of multi-biased ranges observed to a very distant target in a strictly sequential manner. It is impossible to derive the location of the orbiter from such data in a kinematical or geometrical sense without relying heavily on force modeling. LRO orbit determination, therefore, must apply the classical approach to improve a preliminary orbit in an iterative way. The core of this approach is a numerical integration solving simultaneously the equation of motion and the variational equations which provide the partial derivatives for the initial state vector and estimable force model parameters.

For the presented work, the variational equations approach was implemented into the University of Bonn's in-house software originally designed for the purpose of gravity field determination (Mayer-Gürr 2008). The numerical integrator is of Adams-Moulton type and is used for LRO with a stepsize of 10 s. The start values for the initial state vectors are taken from the navigation orbits from the GSFC Flight Dynamics Facility. The integration is performed in an inertial reference frame attached to the mass center of the Moon. This is effected by a shift of the station coordinates for which the lunar ephemeris from DE421 (Williams et al. 2008) is used.

The dynamical modeling of the orbit is based on the GRAIL gravity field model GL0900D (Konopliv et al. 2014) truncated at degree 400. In modeling the tidal forces the solid body tides are computed with the Love number k_2 associated with the gravity field model (0.0239). For the computation of the solar radiation pressure the LRO macromodel published in Smith et al. (2008) is used, for the modeling of the indirect effect together with the lunar albedo model from Floberghagen et al. (1999). For both the direct and indirect radiation, the self-shadowing of the spacecraft components is modeled according to the Sun direction and the orientation of the components (spacecraft body, solar panel, antenna). The 3-D model of the spacecraft needed for this computation was derived from the technical drawings in Tooley (2009). A comprehensive summary of the models used is given in Table 2.

The set of parameters we estimate is largely defined by the properties of the observations as described in the previ-

Table 2 Models used for LRO orbit determination

Modeled effect	Model
<i>Applied to station coordinates</i>	
Earth tides	IERS Conventions 2010 (Petit and Luzum 2010)
Pole tides	IERS Conventions 2010
Ocean tides	IERS Conventions 2010, tide model FES2004
<i>Applied to ranges</i>	
Geocentric light-time correction	IERS Conventions 2010 (for Earth rotation)
Relativistic light-time correction	IERS Conventions 2010 (Sun, Earth, Moon)
Ionospheric delay	IONEX TEC maps from International GNSS Service (IGS)
Tropospheric delay	Vienna Mapping Function (Böhm et al. 2006)
Mass center offset	– 1/0/ – 3 m in S/C system, fixed, estimated from Tooley (2009), p. 28
<i>Force models</i>	
Gravity	GL0900D (Konopliv et al. 2014) up to d/o 400
Direct tides	Sun, Earth, Planets
Solid body tides	Love number $k_2 = 0.0239$ from gravity field model
Solar radiation pressure	Direct and indirect effect, Moon albedo from Floberghagen et al. (1999), Thermal emission from Lemoine et al. (2013), LRO macromodel from Smith et al. (2008), self-shadowing (own development, 3-D model from Tooley 2009, p. 28)
Relativity	Schwarzschild acceleration

Table 3 Parameter set for LRO orbit determination

Parameter type	Range type	Station	Frequency
Initial state vector			Per arc
Range bias	Doppler	All	Per pass
Range drift	Doppler	All	Per pass
Range drift rate	Doppler	White Sands	Per pass
Time bias	Doppler	White Sands	Per arc
Range bias	Two-way	All	Per pass
Time bias	Two-way	All	Per pass
Acceleration along track			Per day
Scale factor solar radiation			Per arc

ous section. Beside the initial state vector it includes a large number of bias parameters, in most cases estimated separately for each pass (Table 3). In addition to the biases with known instrumental background, we also estimate a range drift and a drift rate for the Doppler ranges from White Sands. This choice is purely empirical and will be discussed in the following section.

The parameter set further includes a piecewise linear acceleration along track as frequently applied in orbit determination when the force modeling is known to be incomplete. Finally, a scale factor for the solar radiation pressure is adjusted. This parameter is primarily intended to compensate for the error in the spacecraft mass which is set to a fixed value of 1000 kg since no continuous information on the mass is available. This scale factor will, of course, absorb

errors in the force modeling as well so that both these force parameters have a strong empirical foundation.

An important issue before starting the iteration is the data cleaning. The LRO radio data are, indeed, raw data in the full sense of the term, containing a considerable number of failed observations. This is extremely striking in case of the Doppler ranges, otherwise very smooth with a random noise of a few centimeters. Two types of problems frequently occur:

- At the beginning of a pass, the ranges deviate by hundreds of meters before getting slowly on the right track.
- Across a whole pass, the ranges deviate by tens or hundreds of kilometers.

In particular the latter case is troublesome because one such pass can cause the computation of the entire arc to end in failure. In our experience, more than 10% of the arcs do not converge if bad passes were not removed. Accordingly, our processing starts with an examination of the passes using thresholds for the magnitude of the residuals and the estimate for the range drift. As reference for the examination, again the navigation orbit from the FDF is used. Next, the arc is converged and spurious data are removed. This is done twice, with a restricted and the full parameter set, to minimize the risk of failure.

Between the next and the final iteration, the stochastic modeling is addressed. Up to this time, the data weighting is simplistic, attributing to all observations an accuracy of 10 cm. These weights are now adjusted within a variance compo-

ment estimation (VCE), determining one variance component for each pass. This step accomplishes two tasks:

- A heterogeneous pool of data (two types of ranges from five stations) is provided with realistic weights.
- Passes with undetected issues or large colored noise are downweighted.

The variance components are computed from the weighted residuals and the partial redundancies of the observation groups as described, e.g., in Förstner (1979). This procedure includes itself an iteration which is, of course, not nested with the outer loop of the orbit adjustment. After the arc has converged with equal weights, we suppose that the solution is close enough to the final result to get reliable estimates of the observation errors.

5 Results with short arcs

In applying the strategy described above, we first adopted the design for the arc schedule from the NASA science orbits because it enables a good quality control and keeps the computation effort in reasonable bounds. The nominal arc length was thus chosen to be 2.5 days, each arc starting and ending, if possible, with a sequence of passes observed at White Sands. Subsequent arcs overlap by one such sequence. Along these rules, the 5 years analyzed divided into 884 arcs with 740 overlaps with an average duration of 10.8 hours; further overlaps could not be formed due to maneuvers. For the same reason, 118 arcs start or end at a station other than White Sands.

5.1 Overlap analysis

To discuss the quality of our solution, we divide the 5 years analyzed into six phases by summarizing the more detailed classification used by NASA (Table 4). In Table 5, the overlap analysis for our orbit is shown, separately for these phases and the total average. Following the latter, our orbits achieve a precision of 2.81 m in total position and 0.11 m in radial direc-

Table 4 Classification of the LRO mission

This work	NASA	Period
CO	CO	June 23, 2009–Sept. 6, 2009
NO	NO1–NO13	Sept. 6, 2009–Sept. 16, 2010
SM1	SM1–SM17	Sept. 16, 2010–Dec. 11, 2011
SM2	SM18–SM26	Dec. 11, 2011–Sept. 15, 2012
ES1	ES1–ES11	Sept. 15, 2012–Sept. 18, 2013
ES2	ES12–ES24	Sept. 18, 2013–Sept. 18, 2014

Table 5 Mean RMS values of differences in overlaps of Bonn orbit (arc length 2.5 days), in m

Mission phase	Total	Along	Cross	Radial
CO	4.17	3.12	2.30	0.21
NO	2.02	1.45	1.09	0.06
SM1	2.38	1.84	1.14	0.08
SM2	3.19	2.68	1.19	0.13
ES1	2.92	2.38	1.24	0.14
ES2	3.50	2.77	1.54	0.13
All phases	2.81	2.23	1.28	0.11

Table 6 Mean RMS values of differences between Bonn orbit and NASA science orbit, in m

Mission phase	Total	Along	Cross	Radial
CO	5.02	3.70	2.88	0.29
NO	3.67	2.84	1.94	0.27
SM1	5.82	4.37	3.12	0.58
SM2	5.76	4.61	2.69	0.41
ES1	5.99	4.44	3.32	0.35
ES2	6.80	4.80	3.97	0.50
All phases	5.56	4.17	3.00	0.42

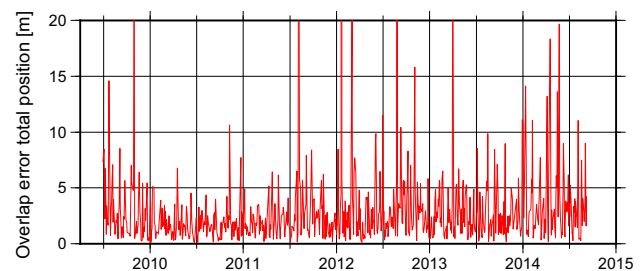


Fig. 2 Overlap errors in total position

tion. These figures are below those reported for the NASA orbits, which are around 10 and 0.5 m, as mentioned in Sect. 1. The direct comparison of the two solutions yields a mean difference of 5.56 m (Table 6), which is less than the uncertainty of the NASA orbits. Our solution is thus consistent with the NASA orbits, but attributed with a higher precision.

The quality assessed for our orbits is indeed less uniform than the averaged values in Table 5 may suggest. It is seen from Fig. 2 that the overlap errors scatter largely throughout the mission, taking values between 11 cm and 41 m. When represented in the orbit reference frame and displayed against the β angle (see Sect. 2), clear correlations with the observation geometry appear (Fig. 3). The directions in the orbit plane (along track and radial) have largest errors in face-on geometry ($\beta = 90^\circ$) when the stations look orthogonally onto the plane. Accordingly, the cross-track direction is best determined in this case. In edge-on geometry, the situation is

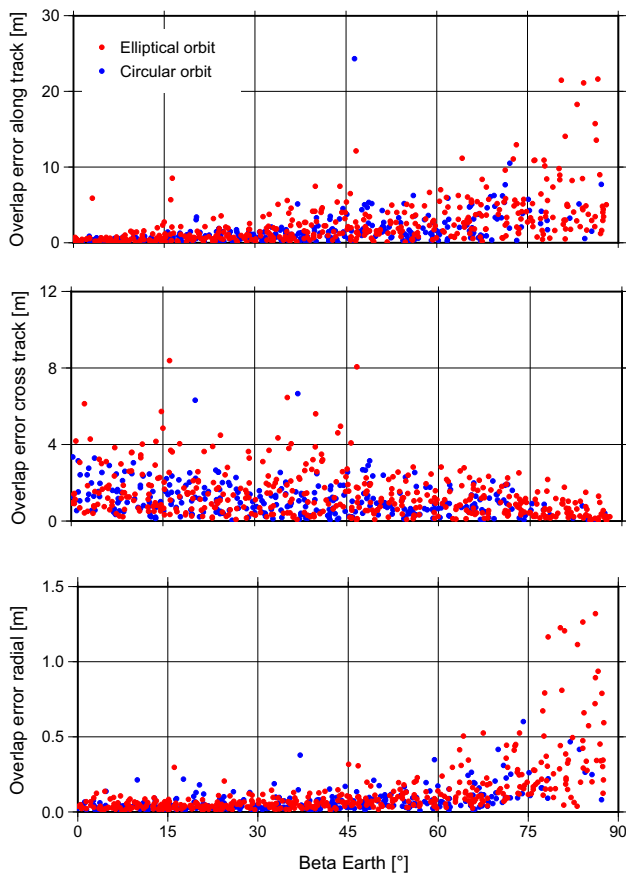


Fig. 3 Overlap errors in orbit system, displayed against Earth viewing angle β . From top to bottom: along track, cross-track, radial. Red: errors in phases CO, SM2, ES1 and ES2 with elliptical orbit, blue: errors in phases NO and SM1 with circular orbit

exactly opposite. Since the error is typically largest in along-track direction, the error in total position is largest in face-on geometry (not shown here).

Another systematics seems to be obvious from Table 5. The phase-averaged errors indicate that our solution is least precise in the short CO phase, seems to be best in NO and SM1 and degrades again between SM1 and SM2, the error in total position increasing by almost 1 m. This sudden rise is emphasized by the phase schedule, because we let SM2 begin when LRO returned to the elliptical orbit (December 11, 2011). Thus, our statistics suggests that the elliptical orbit is more difficult to reconstruct. At first sight, an issue in the force modeling might be suspected, but no such causality could be confirmed.

A closer look at the mission history reveals that the issue is an artifact. As mentioned in Sect. 2, the circular orbit flown in NO and SM1 had to be maintained regularly by SK maneuvers. In order to have the full control over LRO for several hours, these maneuvers were carried out in face-on geometry. When designing the arcs for our analysis, these periods in face-on geometry are then unusable for forming overlaps.

Consequently, only few overlaps at high β angles are available for the circular orbit, as can be seen in Fig. 3. Since this geometry causes the largest errors, the statistics in Table 5 is biased: In contrast to first impression, it does not prove that the elliptical orbit is more challenging, but it is too optimistic concerning the phases NO and SM1. Unfortunately, this bias propagates into the averages over all phases what has to be kept in mind for all statistics below.

5.2 Force parameters

In the following, we discuss some additional results, first the estimates of the force parameters as shown in Figs. 4 and 5. As stated above, both these parameters are expected to absorb a variety of unmodeled effects. In addition, the scale factor for the solar radiation pressure should compensate for the lack of information about the satellite mass. Indeed, its estimates show a distinct upward slope indicating that the fuel reserve has decreased. Roughly estimated, they increase during the 5 years from 0.7 to 0.9. The value for the satellite mass being set to 1000 kg, this corresponds to a decline of the mass from 1400 to 1100 kg which matches well the selective data available. There are, however, abnormal increases with a half-year period, the peaks coinciding with the culmination of the Sun above the orbit plane. They suggest that the solar radiation pressure is amplified when the sunlit part of the orbit outweighs the shadow or no shadow at all occurs. One reason might be the unmodeled thermal reradiation from the orbiter though this effect is expected to be smaller.

The acceleration along track also exhibits unexplained periodical variations. They are more distinct in the phases of the elliptical orbit, also associated with shorter shadow

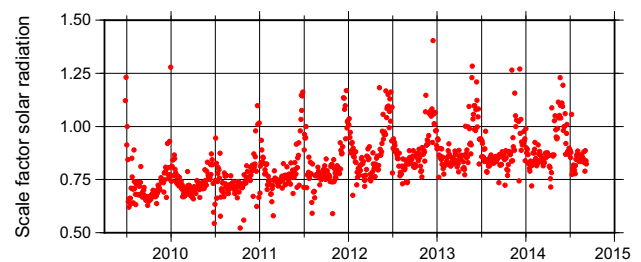


Fig. 4 Estimates of the scale factor for solar radiation pressure

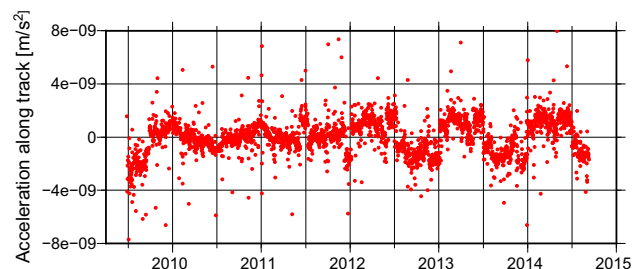


Fig. 5 Estimates of the empirical acceleration along track

passes and, therefore, a higher exposure to the solar radiation. The basic period is 1 year in this case, corresponding to two yaw flip maneuvers needed to restore the orientation of the spacecraft in the orbit plane. Therefore, the reason behind these variations will be again a mismodeling of the radiation pressure, but more in the details of the spacecraft properties. Indeed, a closer analysis shows that some of the variations are related to the orientation of the spacecraft or the motion pattern of the solar panel. However, the estimates of the acceleration are small, at the level of $3 \times 10^{-9} \text{ m/s}^2$, and a better modeling is not likely to improve the orbit very much.

5.3 Observation errors

Though LRO tracking bridges the distance from Earth to Moon, our orbit fit leaves residuals at the sub-meter level.

Table 7 Pass accuracies $\hat{\sigma}$ averaged over observation types and stations (single accuracies weighted with pass lengths)

Station	Antenna size (m)	Doppler ranges (m)	Two-way ranges (m)
White Sands	18	0.01	0.10
Hawaii	13	0.16	0.32
Dongara	13	0.05	0.35
Weilheim	15	0.02	0.21
Kiruna	13	0.07	0.39
All stations		0.03	0.16

Without any doubt, this is favored by the large number of bias parameters which will absorb parts of the observation errors. Nevertheless, an analysis of the residuals gives a differentiated view on the quality of the observations. A convenient tool for that are the variance components providing the accuracy a posteriori for each pass, $\hat{\sigma}$, if multiplied by the accuracy a priori, σ , being set to 10 cm (see Sect. 4).

Along this line, Table 7 shows the accuracies of the passes averaged over observation types and stations, while in Fig. 6 the single accuracies are displayed against the pass length. Unsurprisingly, the VCE attributes lowest errors to the Doppler ranges, in most cases a few centimeters, while the errors of the two-way ranges are larger by one order of magnitude. For the Doppler ranges from White Sands, the estimated error even amounts to just 1 cm. This value is, of course, mainly due to the larger set of bias parameters which includes only for White Sands a drift rate (see Sect. 4). It is obvious, however, that in all Doppler ranges (including White Sands) the error slightly increases with the pass length. This suggests that in longer passes colored noise is still present which cannot be absorbed by the observation model. It may be deduced from this fact that the large variety of bias parameters is also not detrimental for the signal.

With surprising clarity, it is also revealed by the variance components that the performance of the USN stations is not homogeneous. Though the Weilheim station observes the fewest and shortest passes, its observations are assessed to be the most reliable, the Doppler ranges being nearly as

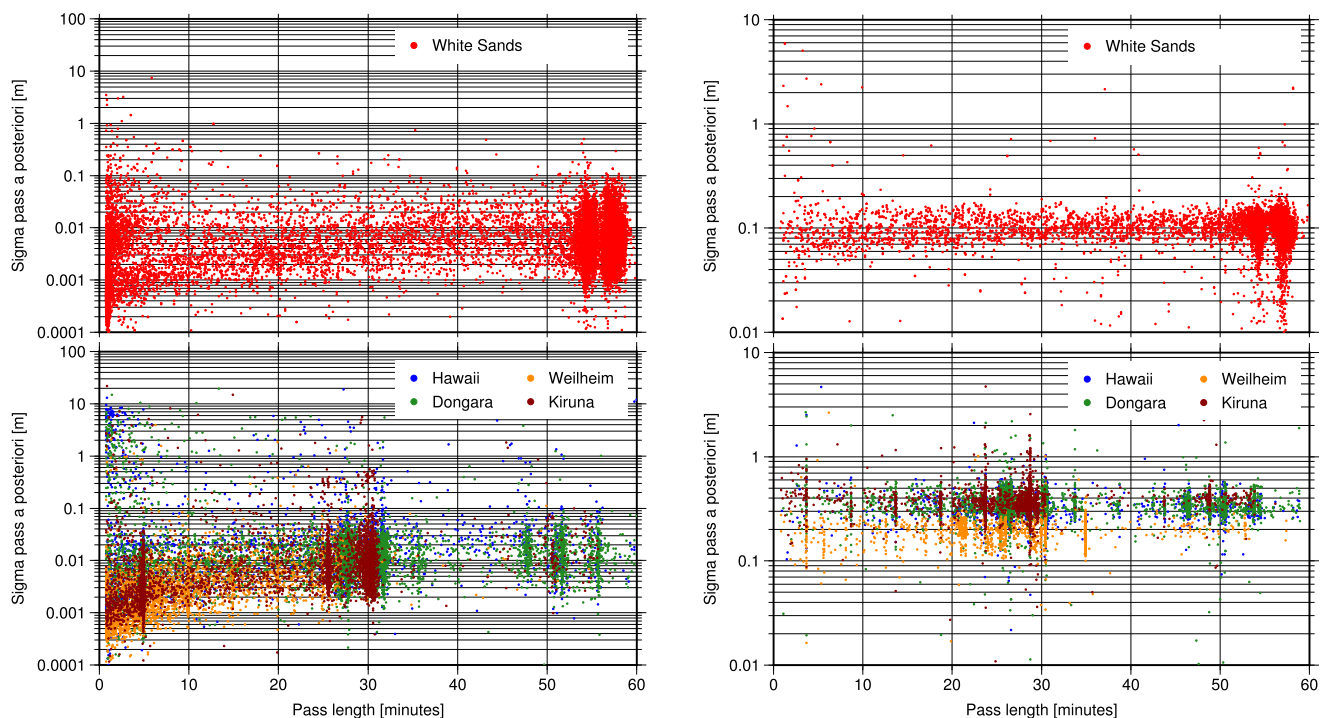


Fig. 6 Pass accuracies $\hat{\sigma}$ from variance component estimation, plotted against the pass length. Left column: Doppler ranges, right column: two-way ranges

Table 8 Estimates of bias parameters found in this work and previous publications. Sources abbreviated as follows: (1) Mazarico et al. (2012), (2) Slojkowski (2014), (3) Mazarico et al. (2017), (4) this work

Parameter	Reported value	Source
Bias Doppler WS	< 0.5 mm/s	1
Bias Doppler USN	− 1 cm/s	2, 3, 4
Time bias Doppler WS	− 13.16 ms until Oct. 2009	1
	− 13.21 ms until Oct. 2009	4
	+ 0.85 ms since Dec. 2010	
Time bias range WS	+ 5 ms	1
	+ 6 to + 7 ms	2
	+ 6 to + 7 ms until Aug. 2013	3
	+ 3 ms since Aug. 2013	
	+ 6.9 ms until Aug. 2013	4
Time bias range USN	+ 3.6 ms since Aug. 2013	
	− 2 to − 4 ms	1
	− 2 ms	2, 4
	− 2 ms until Dec. 2010	3
	− 3 ms since Dec. 2010	

WS White Sands

accurate as those from White Sands. This is probably in line with the technical facts since the Weilheim antenna exceeds the antennas at the other USN stations by 2 m (see Table 7). In contrast, a problem is seen at the Hawaii station whose Doppler ranges are regularly downweighted resulting in an average error two to three times higher than the errors of Dongara and Kiruna.

5.4 Bias parameters

The estimates for the observation biases are, like the force parameters, a secondary outcome of our computation. Since our results partly confirm and partly extend the published values, we briefly report our findings in Table 8, together with those from Mazarico et al. (2012), Slojkowski (2014) and Mazarico et al. (2017). In all bias types, our results agree well with the published values, except for two details. Since December 2010, we notice a small time bias of +0.85 ms in the White Sands Doppler data which is not reported elsewhere. In contrast, we do not see a change in the time bias for the USN ranges as observed by Mazarico et al. (2017).

5.5 Evaluation of processing features

The previous discussion revealed dependencies of the orbits from given facts such as the observation geometry whose change is beyond our control. It might be instructive to see how the orbits depend from decisions we deliberately made during their development. To this end, we computed a small

Table 9 Mean RMS values of differences in overlaps of test solutions, in m

Mission phase	Total	Along	Cross	Radial
<i>Solution S1: no two-way ranges</i>				
CO	4.67	3.49	2.57	0.23
NO	2.30	1.67	1.21	0.08
SM1	2.58	1.99	1.24	0.08
SM2	3.37	2.81	1.27	0.15
ES1	3.14	2.56	1.33	0.15
ES2	4.00	3.25	1.63	0.15
All phases	3.10	2.46	1.38	0.12
Difference to full solution	+ 0.29	+ 0.23	+ 0.10	+ 0.01
<i>Solution S2: no variance component estimation</i>				
CO	18.43	8.11	14.90	0.62
NO	4.13	3.26	1.79	0.16
SM1	5.83	4.84	2.39	0.21
SM2	5.21	4.14	2.11	0.30
ES1	4.03	3.32	1.63	0.23
ES2	5.12	4.07	2.25	0.25
All phases	5.35	4.08	2.50	0.24
Difference to full solution	+ 2.54	+ 1.85	+ 1.22	+ 0.13
<i>Solution S3: no drift and drift rate for White Sands Doppler</i>				
CO	5.65	4.40	3.01	0.23
NO	2.77	1.94	1.60	0.10
SM1	4.54	3.71	1.65	0.14
SM2	4.06	3.29	1.58	0.20
ES1	3.78	3.02	1.63	0.17
ES2	4.36	3.27	2.16	0.15
All phases	3.97	3.10	1.77	0.15
Difference to full solution	+ 1.16	+ 0.87	+ 0.49	+ 0.04
<i>Solution S4: no self-shadowing</i>				
CO	3.78	2.78	2.06	0.18
NO	2.36	1.74	1.25	0.07
SM1	2.77	2.15	1.36	0.08
SM2	3.39	2.79	1.32	0.14
ES1	3.44	2.80	1.43	0.16
ES2	4.04	3.26	1.69	0.14
All phases	3.20	2.53	1.43	0.12
Difference to full solution	+ 0.39	+ 0.30	+ 0.15	+ 0.01

series of test solutions each simplified by suppressing a certain feature of our final processing scheme described above.

The first solution (S1) is based on the Doppler ranges alone, completely ignoring the less accurate two-way ranges. This option was preferred by Maier and Baur (2016) and was also favored for a long time for our orbits. In the second solution (S2), the variance component estimation is omitted. Instead, the observation weights are set to fixed values of 5 cm for the Doppler ranges and 20 cm for the two-way ranges. These values roughly reflect the mean accuracies assessed

with the VCE applied (see Table 7). To avoid excessively bad results, an additional outlier search is performed to remove such passes otherwise rejected by the VCE. The features omitted in two further tests are related to the observation model: In S3 no drift and drift rate are estimated for the White Sands Doppler ranges, and in S4 the solar radiation pressure is computed without considering the self-shadowing of the spacecraft.

The results summarized in Table 9 indicate that none of these modifications cause a dramatic degradation of the orbits. However, given the accuracies of the full solution (2.81 m in total position, 0.11 m radially), the degradation is significant in any case. The largest impact comes from the VCE accounting for an improvement of 2.54 m in total position and 0.13 m in radial direction, meaning that the radial error is lowered by more than 50%. This procedure proves to be extremely useful in the CO phase reducing the error in the position vector from 18.43 to 4.17 m. Obviously, this early phase is characterized by a very inhomogeneous observation material whose properties cannot be described by static weights.

The benefit of the White Sands biases is less than half the size of the VCE (1.16 and 0.04 m, respectively), but still of an order not to be neglected. Utilizing the two-way ranges and considering the self-shadowing effects contribute little to the radial component, otherwise a few decimeters. In both cases, however, the contributions can be larger in single phases. In CO and ES2, for instance, the improvement by the two-way ranges amounts to 0.50 m in total position. The impact of self-shadowing attains the same order in the phases ES1 and ES2.

6 Extending the arc length

As seen in Sect. 5.1, the quality of our solution degrades periodically because of the cyclic changes of the observation geometry. This leads to the idea of decoupling the arcs from these cycles by extending the arc length, so that no single arc is hampered by a bad geometry from start to end. This will not eliminate the problem that the orbit is badly determined in such phases, but at least a more uniform distribution of the errors should result. The best we can hope is that the constraints from observations collected in good geometry are strong enough to tighten the orbit where the geometry is bad. This strategy is, of course, not without risks because the transition to longer arcs will be accompanied by an accumulation of the errors in the force models. This point is critical for any Earth satellite and should be most critical for LRO.

In the solutions presented here we confined ourselves, therefore, to a maximum arc length of 10.5 days scaled from the short arc solution in steps of 2 days. The processing strategy was the same as applied in the previous sections except a detail in the arc scheduling we address below. The results

Table 10 Mean RMS values of differences in overlaps of solutions with extended arc length, in m

Mission phase	Total	Along	Cross	Radial
<i>Solution E1: arc length 4.5 days</i>				
CO	4.02	3.05	1.90	0.26
NO	1.73	1.27	0.91	0.07
SM1	1.43	1.07	0.82	0.08
SM2	1.95	1.57	0.87	0.17
ES1	2.82	2.36	1.02	0.21
ES2	2.81	2.41	0.97	0.17
All phases	2.21	1.78	0.96	0.14
Diff. to solution from 2.5 days	−0.60	−0.45	−0.32	+0.03
<i>Solution E2: arc length 6.5 days</i>				
CO	2.96	2.26	1.37	0.33
NO	1.82	1.31	0.89	0.07
SM1	1.36	0.74	1.00	0.07
SM2	2.42	2.03	0.85	0.23
ES1	2.23	1.79	0.88	0.20
ES2	2.88	2.36	1.23	0.21
All phases	2.15	1.69	0.98	0.16
Diff. to solution from 2.5 days	−0.66	−0.58	−0.30	+0.05
<i>Solution E3: arc length 8.5 days</i>				
CO	3.52	2.91	1.46	0.33
NO	1.07	0.66	0.72	0.07
SM1	1.15	0.60	0.94	0.08
SM2	1.37	1.02	0.73	0.17
ES1	2.72	2.28	1.00	0.25
ES2	3.06	2.57	1.17	0.25
All phases	1.99	1.53	0.94	0.17
Diff. to solution from 2.5 days	−0.82	−0.70	−0.34	+0.06
<i>Solution E4: arc length 10.5 days</i>				
CO	2.67	2.43	0.84	0.35
NO	1.18	0.80	0.83	0.09
SM1	1.22	0.94	0.75	0.06
SM2	3.66	3.41	0.62	0.26
ES1	2.52	2.19	0.97	0.26
ES2	2.52	2.10	1.06	0.25
All phases	2.13	1.80	0.85	0.18
Diff. to solution from 2.5 days	−0.68	−0.43	−0.43	+0.07

shown in Table 10 apparently confirm the considerations expressed above. The 5-year average of the position error decreases step by step attaining 1.99 m at 8.5 days, 0.82 m below the solution from 2.5 days. This trend does not continue until the last solution, the error with 10.5 days being again at the level of 6.5 days. The improvement up to 8.5 days is mainly due to smaller errors in the along-track direction, as could be expected. The radial direction does not improve, its errors even increase by a few centimeters. Interestingly, the errors do not drop continuously in some mission phases

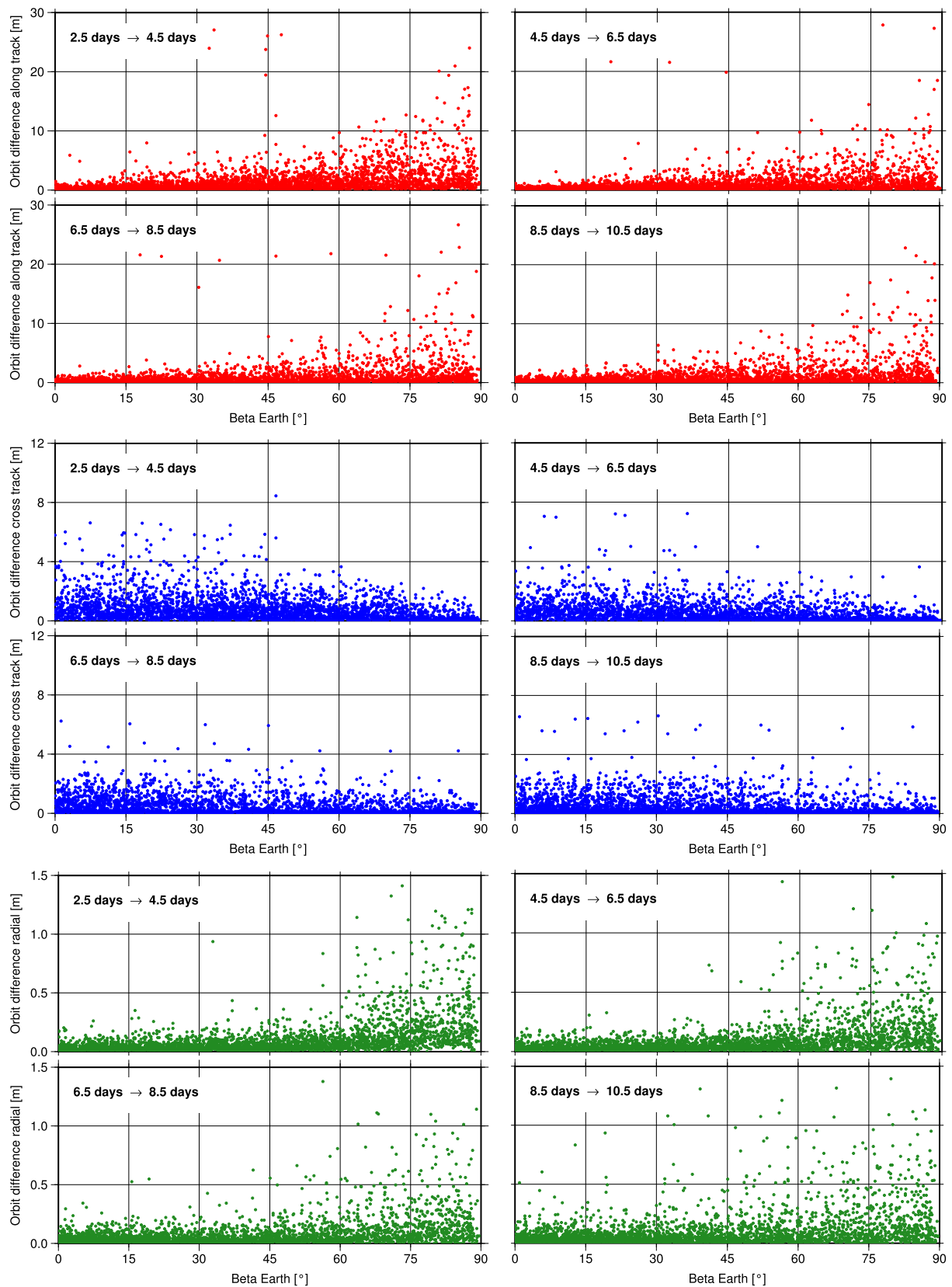


Fig. 7 Changes in orbit solutions when extending the arc length from 2.5 to 10.5 days in steps of 2 days. Daily RMS values of the position differences in orbit system displayed against Earth viewing angle β . From top to bottom: along track (red), cross-track (blue), radial (green)

showing that the use of longer arcs comes along with uncertainties.

The results in Table 10, altogether rather satisfying, should be viewed with caution for two reasons. First, the number of overlapping periods decreases rapidly with the increase of the arc length. From 740 in the short arc solution, it drops to 336 with arcs of 4.5 days and finally to 121 when dividing the orbit into arcs of 10.5 days. Thus, the reliability of our statistics becomes weaker and weaker. Second, a uniform length of the overlaps is more difficult to obtain with longer arcs. In filling the time between two maneuvers with arcs of the nominal length, more often a short period is left so that, if priority is given to uniform overlaps, very long and very short arcs would be mixed. To avoid this, we let the last arc in such periods also have the nominal arc length leading to many overlaps with a length of several days. This also reduces the significance of the statistics.

The first of these issues cannot be resolved, the second not without contradictions. Therefore, we try to support our statistics by a comparison of the solutions over the full 5 years introducing our knowledge gained with the overlaps in the short arc solution. Assuming that the solutions really improve with increasing arc length, we should expect that the well determined parts of the orbit are kept and the changes take place where the geometry is bad. Moreover, the magnitude of these changes should decrease the closer the solutions come to the true orbit. In other words, extending the arc length step by step should result in a series of solutions showing a convergent behavior.

To verify these considerations, we compared our solutions pairwise as neighbored in the series of arc lengths from 2.5 to 10.5 days. The orbit differences were computed as done in the overlap analysis and averaged to daily RMS values. Finally, the daily RMS were assigned to the β angle of the day. Figure 7 shows that way the changes in the solutions separately for the components of the orbit system. As expected, the directions observed under a favorable geometry are nearly left unchanged when extending the arc length. The largest differences are found where the geometry is weak: at $\beta = 90^\circ$ in the along-track direction and radially and at $\beta = 0^\circ$ in the cross-track direction. It is obvious, therefore, that the longer arcs at least conserve the precision of the short arc solution. Beyond that, the comparisons suggest that the solutions improve because there are signs of convergence. The changes in the along-track direction clearly decrease in magnitude up to an arc length of 8.5 days. The same can be observed, with some lesser clarity, in the cross-track direction. No further decrease can be found in the last step to 10.5 days and no decrease at all in the radial direction. These results are fully in line with the overlap statistics suggesting that a constant improvement of the orbit up to an arc length of 8.5 days is possible.

7 Conclusions

We presented 5 years of orbits of the Lunar Reconnaissance Orbiter from S-band Doppler and range data computed independently from NASA using an own software development. Assessed by an analysis of overlapping arcs, the precision of the orbits was found to be 2.81 m in total position and 0.11 m in the radial direction based on an arc length of 2.5 days. Given these figures, our orbits seem to be at the same level with the NASA science orbits. Referred to the accuracies published for the NASA orbits (10 and 0.5 m, respectively), the figures above even indicate a substantial improvement.

It is unclear whether further refinements of the orbits would be possible or required. Even if the overlap analysis turned out to be too optimistic for some mission phases, the precision achieved in the radial direction seems to come close to the performance of the LOLA altimeter (10 cm). Our orbits should thus allow to recover more or even the full signal in the LOLA ranges including the signature of the lunar body tides. The presence of this signature in the LOLA data was proven in Mazarico et al. (2014) using the NASA science orbits, already with impressive results.

The accuracies in the horizontal directions are still clearly behind the resolution of the instruments, in particular of the LROC narrow-angle cameras (50 cm). It is indeed more than doubtful whether such a precision is ever attainable. The main obstacle seems to be the observation geometry changing periodically with the motion of the Moon. By using longer arcs, we could mitigate this effect to some extent, but further improvements are not likely that way.

8 Distribution of the orbits

The orbits presented in this paper are available at the website of the University of Bonn (<https://www.apmg.uni-bonn.de/daten-und-modelle/lro-orbits>). For convenient use in existing applications, they are provided as sets of SPICE kernels adopting the classification of the mission phases used for the NASA science orbits.

Acknowledgements This research was funded by the German Research Foundation (DFG) within the research unit FOR 1503 “Space-Time Reference Systems for Monitoring Global Change and for Precise Navigation in Space”. We thank three anonymous reviewers for their thoughtful and constructive comments.

References

- Bauer S, Hussmann H, Oberst J, Dirkx D, Mao D, Neumann G, Mazarico E, Torrence M, McGarry J, Smith D, Zuber M (2017) Analysis of one-way laser ranging data to LRO, time transfer and clock characterization. *Icarus* 283:38–54. <https://doi.org/10.1016/j.icarus.2016.09.026>

- Böhm J, Werl B, Schuh H (2006) Troposphere mapping functions for GPS and very long baseline interferometry from European Centre for Medium-Range Weather Forecasts operational analysis data. *J Geophys Res* 111:B02406. <https://doi.org/10.1029/2005JB003629>
- Chin G, Brylow S, Foote M, Garvin J, Kasper J, Keller J, Litvak M, Mitrofanov M, Paige D, Raney K, Robinson M, Sanin A, Smith D, Spence H, Spudis P, Stern S, Zuber M (2007) Lunar Reconnaissance Orbiter overview: the instrument suite and mission. *Space Sci Rev* 129:391–419. <https://doi.org/10.1007/s11214-007-9153-y>
- Floberghagen R, Visser P, Weischede F (1999) Lunar albedo force modeling and its effect on low lunar orbit and gravity field determination. *Adv Space Res* 23(4):733–738. [https://doi.org/10.1016/S0273-1177\(99\)00155-6](https://doi.org/10.1016/S0273-1177(99)00155-6)
- Förstner W (1979) Ein Verfahren zur Schätzung von Varianz- und Kovarianzkomponenten. *Allg Vermess* 11–12:446–453
- GSFC (2010) Station raw tracking data. http://pds-geosciences.wustl.edu/lro/lro-l-rss-1-tracking-v1/lrors_0001/document/lro_desc_trk.txt
- Keller J, Petro N, Vondrak R (2016) The Lunar Reconnaissance Orbiter mission: six years of science and exploration at the Moon. *Icarus* 273:2–24. <https://doi.org/10.1016/j.icarus.2015.11.024>
- Konopliv A, Park R, Yuan D, Asmar S, Watkins M, Williams J, Fahnestock E, Kruizinga G, Paik M, Strelakov D, Harvey N, Smith D, Zuber M (2014) High-resolution lunar gravity fields from the GRAIL primary and extended missions. *Geophys Res Lett* 41:1452–1458. <https://doi.org/10.1002/2013GL059066>
- Lemoine F, Goossens S, Sabaka T, Nicholas J, Mazarico E, Rowlands D, Loomis B, Chinn D, Caprette D, Neumann G, Smith D, Zuber M (2013) High degree gravity models from GRAIL primary mission data. *J Geophys Res Planets* 118:1676–1698. <https://doi.org/10.1002/jgre.20118>
- Löcher A, Hofmann F, Gläser P, Haase I, Müller J, Kusche J, Oberst J (2017) Towards improved lunar reference frames: LRO orbit determination. In: van Dam T (ed) REFAG 2014, International Association of Geodesy Symposia. Springer, Berlin, pp 201–207. https://doi.org/10.1007/1345_2015_146
- LRO Radio Science Archive (n.d.) http://pds-geosciences.wustl.edu/lro/lro-l-rss-1-tracking-v1/lrors_0001/
- Maier A, Baur O (2016) Orbit determination and gravity field recovery from Doppler tracking data to the Lunar Reconnaissance Orbiter. *Planet Space Sci* 122:94–100. <https://doi.org/10.1016/j.pss.2016.01.014>
- Mao D, McGarry J, Mazarico E, Neumann G, Sun X, Torrence M, Zagwodzki T, Rowlands D, Hoffman E, Horvath J, Golder J, Barker M, Smith D, Zuber M (2017) The laser ranging experiment of the Lunar Reconnaissance Orbiter: five years of operations and data analysis. *Icarus* 283:55–69. <https://doi.org/10.1016/j.icarus.2016.07.003>
- Mayer-Gürr T (2008) Gravitationsfeldbestimmung aus der Analyse kurzer Bahnbögen am Beispiel der Satellitenmissionen CHAMP und GRACE. Dissertation, University of Bonn
- Mazarico E, Rowlands D, Neumann G, Smith D, Torrence M, Lemoine F, Zuber M (2012) Orbit determination of the Lunar Reconnaissance Orbiter. *J Geod* 86(3):193–207. <https://doi.org/10.1007/s00190-011-0509-4>
- Mazarico E, Lemoine F, Goossens S, Sabaka T, Nicholas J, Rowlands D, Neumann G, Torrence M, Smith D, Zuber M (2013) Improved precision orbit determination of lunar orbiters from GRAIL-derived lunar gravity models. In: Proceedings of the 23rd AAS/AIAA Space Flight Mechanics Meeting, San Diego CA, pp 1125–1141
- Mazarico E, Barker M, Neumann G, Zuber M, Smith D (2014) Detection of the lunar body tide by the Lunar Orbiter Laser Altimeter. *Geophys Res Lett* 41(7):2282–2288. <https://doi.org/10.1002/2013GL059085>
- Mazarico E, Neumann G, Barker M, Goossens S, Smith D, Zuber M (2017) Orbit determination of the Lunar Reconnaissance Orbiter: status after seven years. *Planet Space Sci*. <https://doi.org/10.1016/j.pss.2017.10.004>
- Nicholson A, Slojkowski S, Long A, (2010) NASA GSFC Lunar Reconnaissance Orbiter (LRO) orbit estimation and prediction. SpaceOps, Huntsville, Alabama. <https://doi.org/10.2514/6.2010-2328>
- Petit G, Luzum B (2010) IERS Conventions. IERS Technical Note 36. Verlag des Bundesamts für Kartographie und Geodäsie, Frankfurt am Main
- Robinson M, Brylow S, Tschimmel M, Humm D, Lawrence S, Thomas P, Denevi B, Bowman-Cisneros E, Zerr J, Ravine M, Caplinger M, Ghaemi F, Schaffner J, Malin M, Mahanti P, Bartels A, Anderson J, Tran T, Eliason E, McEwen A, Turtle E, Jolliff B, Hiesinger H (2010) Lunar Reconnaissance Orbiter Camera (LROC) instrument overview. *Space Sci Rev* 150:81–124. <https://doi.org/10.1007/s11214-010-9634-2>
- Slojkowski S (2014) Lunar Reconnaissance Orbiter orbit determination accuracy analysis. In: 24th International Symposium on Space Flight Dynamics, Laurel, Maryland. <https://ntrs.nasa.gov/archive/nasa/casi.ntrs.nasa.gov/20140008968.pdf>
- Smith D, Zuber M, Lemoine F, Torrence M, Mazarico E (2008) Orbit determination of LRO at the Moon. In: 16th International Workshop on Laser Ranging, Poznan, Poland
- Smith D, Zuber M, Jackson G, Cavanaugh J, Neumann G, Riris H, Sun X, Zellar R, Coltharp C, Connelly J, Katz B, Kleyner I, Liiva P, Matuszeski A, Mazarico E, McGarry J, Novo-Gradac A, Ott M, Peters C, Ramos-Izquierdo L, Ramsey L, Rowlands D, Schmidt S, Scott V, Shaw G, Smith J, Swinski J, Torrence M, Unger G, Yu A, Zagwodzki T (2010) The Lunar Orbiter Laser Altimeter investigation on the Lunar Reconnaissance Orbiter Mission. *Space Sci Rev* 150:209–241. <https://doi.org/10.1007/s11214-009-9512-y>
- Tooley C (2009) Lunar Reconnaissance Orbiter mission update. Werner von Braun Memorial Symposium 2009, Huntsville, Alabama. http://astronautical.org/sites/default/files/vonbraun/2009/VonBraun_Symposium_2009-10-20_4a_Tooley.pdf
- Vondrak R, Keller J, Chin G, Garvin J (2010) Lunar Reconnaissance Orbiter (LRO): observations for lunar exploration and science. *Space Sci Rev* 150:7–22. <https://doi.org/10.1007/s11214-010-9631-5>
- Williams J, Boggs D, Folkner W (2008) DE421 lunar orbit, physical librations, and surface coordinates. JPL Interoffice Memorandum 335-JW,DB,WF-20080314-001
- Zuber M, Smith D, Lehman D, Hoffman T, Asmar S, Watkins M (2013) Gravity Recovery and Interior Laboratory (GRAIL): mapping the lunar interior from crust to core. *Space Sci Rev* 178:3–24. <https://doi.org/10.1007/s11214-012-9952-7>